



Mitigating amorphization in superhard boron carbide by microalloying-induced stacking fault formation

Qi An ^{*}

Department of Chemical and Materials Engineering, University of Nevada-Reno, Reno, Nevada 89577, USA

 (Received 5 May 2021; revised 16 September 2021; accepted 28 September 2021; published 12 October 2021)

The abnormal brittle failure of superhard boron carbide (B_4C) and other icosahedral solids arises from the shear-induced amorphization. Mitigating the amorphization in these materials remains challenging due to the lack of other deformation mechanisms such as mobile dislocations. This paper illustrates the shear-induced amorphization process of B_4C from molecular dynamics (MD) simulations using quantum-mechanics-derived machine-learning force field. The amorphization in B_4C initiates from the disintegration of icosahedral clusters, and then this icosahedral deconstruction propagates and merges to form an amorphous region with 2–3 nm in width, leading to the following cavitation and brittle failure. More interesting, the deformation mechanism transforms from amorphization to stacking fault (SF) formation by microalloying aluminum (Al) into B_4C . This SF formation originates from the enhanced icosahedral slip as the Al is incorporated into the C-B-C chain to form a C-Al-C chain. This paper illustrates a deformation mechanism of superhard icosahedral solids and provides a strategy for suppressing the amorphization and brittle failure of B_4C .

DOI: [10.1103/PhysRevMaterials.5.103602](https://doi.org/10.1103/PhysRevMaterials.5.103602)

I. INTRODUCTION

Boron carbide (B_4C) is extremely hard with a high Hugoniot elastic limit, yet it has a low density of $\sim 2.5 \text{ g/cm}^3$ due to the unique crystal structure consisting of B_{12} -based icosahedral motifs and a three-atom chain [1,2]. These outstanding physical properties make B_4C a promising material for personal body armor and other protection applications [3–5]. However, B_4C suffers from abnormal brittle failure just exceeding the elastic limit, preventing it from extensive engineering applications [6]. This brittle failure is directly related to the amorphous shear band formation (2–3 nm in width and several hundred nanometers in length), which is observed in many mechanical experiments such as hypervelocity impact [7], nanoindentation [8], shock compression [9], scratching [10], as well as ion irradiation [11]. Recent theoretical studies significantly advanced the understanding of the deformation mechanism and the amorphous band formation in B_4C [12–16]. Density functional theory (DFT) simulations on the shear deformation of B_4C along 11 plausible slip systems indicated that the shear-induced failure process initiates from the deconstruction of icosahedral clusters due to the interaction of cage and C-B-C chain [12]. In addition, we applied reactive force field (ReaxFF) molecular dynamics (MD) simulations to demonstrate that the formation of the amorphous band arises from the deconstruction of icosahedral clusters under shear deformation [13]. The amorphous region has a higher density than the nearby crystalline region, leading to negative pressure and cavitation within the amorphous region [13]. Despite extensive experimental and theoretical studies, the amorphization process in B_4C remains not fully understood, especially the detailed propagation of amorphization

along the shear band. Illustrating the amorphization process in B_4C provides an important basis for design of hard yet ductile materials in the future.

Amorphization is related to the cavitation and brittle failure of B_4C and other icosahedral solids [12,17]. Therefore, mitigating this phase transition is essential to enhance their ductility. To mitigate the amorphization in B_4C , many strategies have been proposed in recent studies [18] including dopant [19], B/C stoichiometry control [20], second phase addition [21], and grain boundary (GB) engineering [22]. Experimentally, Xiang *et al.* [19] demonstrated that doping 1–2% Si into B_4C decreases the amorphization by up to $\sim 30\%$, while it increases the fragmentation and microcracking. Another effective approach is to increase the B/C ratio, resulting in higher strength and decreased amorphization [20]. Furthermore, less fracture is observed by adding the reinforcement particles, such as SiC, TiC, TiB_2 , and Al_2O_3 , into B_4C [23–25]. In addition, we showed that GB sliding can improve the ductility of nanocrystalline B_4C by performing ReaxFF MD simulations on supercells of millions of atoms [22]. In addition to the above approaches, an interesting strategy is proposed based on the shear-induced failure process investigated from DFT simulations [12]. The deconstruction of the icosahedral cluster initiates from the active interaction between the middle B in the C-B-C chain and the icosahedral cluster under shear deformation [12]. Therefore, we suggested that replacing the three-atom chain with a two-atom chain can facilitate the icosahedral slip in B_4C without breaking the icosahedral cage. This modification has been demonstrated to be effective using DFT simulations on $(B_{12}P_2)$ [26] and $(B_{11}C)Si_2$ [27]. However, it has not been demonstrated for realistic systems because of the limitation size of DFT simulations (~ 100 atoms) as well as the lack of temperature effects in DFT simulations.

^{*}Corresponding author: qia@unr.edu

In this paper, an accurate machine-learning force field (ML-FF) is developed for both B_4C and Al-doped B_4C systems based on extensive quantum mechanics (QM) simulations. Then the amorphization and brittle failure mechanism of B_4C are illustrated from the MD simulations using this ML-FF. The simulation results indicate that the shear-induced amorphization in B_4C arises from deconstructing icosahedra along a shear plane, yet it is confined to two icosahedral layers in the beginning. Then the amorphization propagates to two opposite directions and transforms to other neighbor icosahedral layers. Next, the propagation of amorphization along parallel icosahedral layers merges to form an amorphous region with 2–3 nm in width. Finally, a cavity is present in this region, leading to brittle failure. More important, a realistic design strategy is proposed to mitigate the amorphization and demonstrated by the ML-FF MD simulations. Substituting the C-B-C chain with the C-Al-C chain transforms the deformation mechanism from amorphization to stacking fault (SF) formation due to the enhanced icosahedral slip without disintegrating the icosahedral clusters. The present results indicate that microalloying Al is effective to activate the alternative deformation mechanism other than amorphization in B_4C and other icosahedral solids. The activation of the SF formation mechanism is expected to drastically enhance the ductility of B_4C .

II. COMPUTATIONAL METHODS

A. QM simulations

The QM-MD simulations were performed to generate the training set for developing the ML-FF. The atomic force, the energy, and the virial stress tensor for the simulation systems were derived from the QM-MD trajectory. All QM-MD simulations were performed using VASP software based on the plane-wave basis set [28–31]. In the QM-MD simulations, the cell parameters were allowed to relax to adjust the external pressure using the isobaric-isothermic (NPT) ensemble. The temperature and pressure were controlled using the Langevin thermostat [32] and the Parrinello-Rahman barostat [33], respectively. The canonical (NVT) ensemble was adopted for the fixed volume simulations with just the Langevin thermostat. A timestep of 1.0 fs was applied in integrating the equations of motion in all QM-MD simulations.

The forces on each atom were calculated using DFT. The Perdew-Burke-Ernzerhof functional was adopted to account for the exchange-correlation interaction [34,35]. In QM-MD simulations, the energy cutoff for plane-wave expansion and the energy convergence for the self-consistent field were set up to 400 eV and 1.0×10^{-4} eV, respectively. The sampling of the first Brillouin zone was performed using the Γ -point only approach. To account for the partial occupancy of electrons, the Gaussian smearing method was adopted, and the width for the smearing was 0.05 eV.

B. The development of ML-FF

To develop an accurate FF for describing both B_4C and Al-doped B_4C [(B_{12})CAIC], a large training set was generated from QM-MD simulations. Particularly, the training set included following structures: (1) boron carbide (B_4C); (2)

(B_{12})CAIC; and (3) elementary boron phases such as α - B_{12} [36], β - B_{106} [37], β - B_{105} [37], τ - B_{212} [38], and γ - B_{28} [39].

Extensive QM-MD data were included for the most stable configuration ($B_{11}C_p$)CBC. These QM data included (1) the heating process of crystalline phase from 300 to 4300 K within 40 ps, leading to the liquid phase; (2) the continuous quenching process of the liquid phase from 4300 to 300 K within 40 ps, leading to the formation of the amorphous phase; (3) the equation of state for both crystalline and amorphous phases at 300 K; equilibrium lattice parameters were uniformly compressed to 0.98, 0.96, 0.94, and 0.92 of original lattice, and were increased to 1.02 and 1.05 of original lattice, and then the system was equilibrated for 10 ps using NVT; (4) the crystalline phase at 300, 500, 1000, 1500, 2000, 2500, 3000, and 3500 K for 10 ps; (5) the liquid (or amorphous) phase at 300, 500, 1000, 1500, 2000, 2500, 3000, 3500, 4000, and 4300 K for 10 ps; and (6) the shear deformation configuration along the (001)[100] slip system at 300 K for 10 ps. For the high-energy configurations (B_{12})CCC and ($B_{11}C_e$)CBC, the training set included the crystal at room temperature for 10 ps, as well as the heating process from 300 to 4300 K in 40 ps. To account for the possible twinning formation in a shear deformation, the τ - B_4C structure [40] was also included in the training set. For the asymmetric twin structure, the modified τ - B_4C with half ($B_{11}C_p$)CBC and half ($B_{11}C_e$)CBC was included. The boron-rich boron carbide ($B_{13}C_2$) was also included. For the τ - B_4C , modified τ - B_4C , $B_{13}C_2$, and elementary boron phases (α - B_{12} , β - B_{106} , β - B_{105} , τ - B_{212} , γ - B_{28}), the QM-MD simulations are (1) crystal phase at 300 K for 10 ps; (2) heating from 300 to 4300 K for 40 ps; and (3) quenching from 4300 to 300 K for 40 ps. For the (B_{12})CAIC, the training set included the same QM-MD simulations as the ($B_{11}C_p$)CBC, which provided a good training set for an accurate description of this Al-doped B_4C .

In the ML-FF training process, a cutoff radius for neighbor searching was set up to 5.2 Å and the smoothing starts from 5.0 Å. The size of the three layers of neural networks was 120 in the fitting process. The learning rate varied from 0.001 to 3.51×10^{-8} with an exponential decay in the total of 1 000 000 training steps. The loss function was composed of energy error, force error, and virial error, and the evolution of the loss function is shown in Fig. S1 of the Supplemental Material (SM) [41].

C. MD simulations using ML-FF

The MD simulations were performed using LAMMPS software [42] with the ML-FF applied to describe the interatomic interactions. The velocity Verlet algorithm was used for integrating the equations of motion with a timestep of 1.0 fs in all MD simulations. The possible surface effects were eliminated by periodic boundary conditions (PBCs) along with three directions. The NPT ensemble was applied in all simulations with the Noose-Nover thermostat and barostat for controlling the temperature and pressure, respectively. The damping constants were 0.2 and 2.0 ps for thermostat and barostat, respectively.

The bulk modulus and shear modulus were computed using the Voigt-Reuss-Hill average from the elastic constants C_{ij} and stiffness constants S_{ij} [43]. The lattice of the supercell

was deformed elastically along possible directions to derive the elastic constant C_{ij} [44]. The inversion of the C_{ij} matrix is the S_{ij} . A $4 \times 4 \times 4$ rhombohedral supercell with 960 atoms was used for the elastic modulus calculations for both $(B_{11}C_p)CBC$ and $(B_{12})CAIC$.

For the finite shear simulations, a larger $24 \times 24 \times 6$ supercell with 51 840 atoms was used for both $(B_{11}C_p)CBC$ and $(B_{12})CAIC$. The systems were equilibrated at 300 K for 100 ps before shear simulation. The temperature and atomic stress were calculated for each atom in the simulation cell during the shear simulation. The stress tensor was computed using the virial theorem, as shown in Eq. (1), where m , v , r , and f correspond to atomic mass, velocity, position, and force, respectively [45]. Then these physical properties were coarse-grained using $\sim 1 \times 1$ nm bins (~ 300 atoms) in the $x - y$ plane to illustrate the temperature, pressure, and shear stress evolution during the amorphization. The binning analysis is along lattice a and b so that the results are rectangular meshed:

$$\sigma_{xy} = \frac{1}{V} \left[\sum_j m_j v_{jx} v_{jy} + \frac{1}{2} \sum_{i \neq j} r_{ijx} f_{ijy} \right] \quad (1)$$

III. RESULTS AND DISCUSSION

A. The validation of the ML-FF

To demonstrate the accuracy of the ML-FF, the structural and mechanical properties of B_4C were computed and compared with DFT and experimental results. The ML-FF predicts the lattice parameters of $a = 5.212 \text{ \AA}$, $b = 5.069 \text{ \AA}$, $c = 5.221 \text{ \AA}$, $\alpha = 66.02^\circ$, $\beta = 65.23^\circ$, and $\gamma = 65.97^\circ$ for B_4C , agreeing well with the DFT values at 0 K [12]. For $(B_{12})CAIC$, the lattice parameters are $a = 5.355 \text{ \AA}$, $b = 5.344 \text{ \AA}$, $c = 5.289 \text{ \AA}$, $\alpha = 64.17^\circ$, $\beta = 64.19^\circ$, and $\gamma = 63.67^\circ$ from ML-FF at room temperature, which also agree well with DFT values at 0 K ($a = b = 5.347 \text{ \AA}$, $c = 5.261 \text{ \AA}$, $\alpha = \beta = 64.28^\circ$, $\gamma = 63.56^\circ$). The ML-FF predicts a density of 2.51 g/cm^3 for B_4C at room temperature, which agrees very well with experiment (2.52 g/cm^3) [2] and DFT value (2.53 g/cm^3 at 0 K) [12]. In addition, the bulk modulus (K) and shear modulus (G) are predicted to be 241 and 191 GPa for B_4C , well consistent with experiment (K = 235 GPa

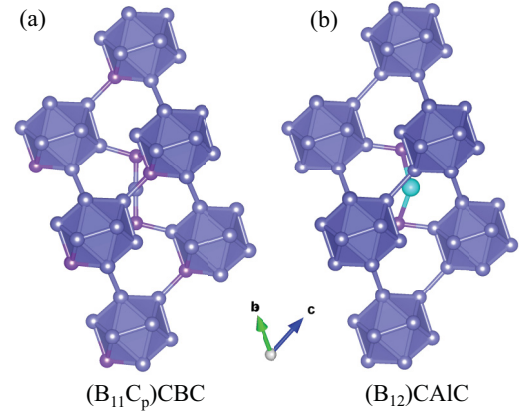


FIG. 1. The atomistic structure of B_4C and Al-doped B_4C . (a) The ground state structure $(B_{11}C_p)CBC$. (b) The lowest energy structure $(B_{12})CAIC$. The B, C, and Al are represented by light blue, purple, and cyan balls, respectively.

and $G = 197 \text{ GPa}$) and DFT values (K = 238 GPa and $G = 199 \text{ GPa}$) [12]. The summary of lattice parameters and elastic modulus is in Table I below.

B. Amorphization of B_4C under shear deformation

The crystalline B_4C consists of icosahedral clusters connected by the three-atom chains along the $[111]$ rhombohedral direction [Fig. 1(a)]. The ground state structure has $(B_{11}C_p)$ icosahedra which are bonded to the C-B-C chain through equatorial (e) sites and are linked to other icosahedra via polar (p) sites [12]. This paper focuses on the finite shear deformation of the ground state structure $(B_{11}C_p)CBC$ along the slip system $(001)[100]$ (the three-index rhombohedral notation is used to represent the slip plane and direction in this paper). This slip system is selected because it is the most plausible slip system in B_4C from our DFT simulations on 11 plausible slip systems [12]. Therefore, it is the most plausible to be activated under applied stress conditions, leading to the amorphization. Indeed, the amorphization along this slip system was observed

TABLE I. Lattice parameters and elastic modulus of $(B_{11}C_p)CBC$ and $(B_{12})CAIC$ from DFT and ML-FF simulations.

	$(B_{11}C_p)CBC$		$(B_{12})CAIC$	
	Lattice parameters	Elastic modulus	Lattice parameters	Elastic modulus
DFT (0 K)	$a = 5.207 \text{ \AA}$, $b = 5.057 \text{ \AA}$, $c = 5.207 \text{ \AA}$, $\alpha = 66.01^\circ$, $\beta = 65.16^\circ$, $\gamma = 66.01^\circ$	K = 238 GPa, G = 199 GPa	$a = b = 5.347 \text{ \AA}$, $c = 5.261 \text{ \AA}$, $\alpha = \beta = 64.28^\circ$, $\gamma = 63.56^\circ$	K = 225 GPa, G = 197 GPa
ML-FF (300 K)	$a = 5.212 \text{ \AA}$, $b = 5.069 \text{ \AA}$, $c = 5.221 \text{ \AA}$, $\alpha = 66.02^\circ$, $\beta = 65.23^\circ$, $\gamma = 65.97^\circ$	K = 241 GPa, G = 191 GPa	$a = 5.355 \text{ \AA}$, $b = 5.344 \text{ \AA}$, $c = 5.289 \text{ \AA}$, $\alpha = 64.17^\circ$, $\beta = 64.19^\circ$, $\gamma = 63.67^\circ$	K = 233 GPa, G = 181 GPa

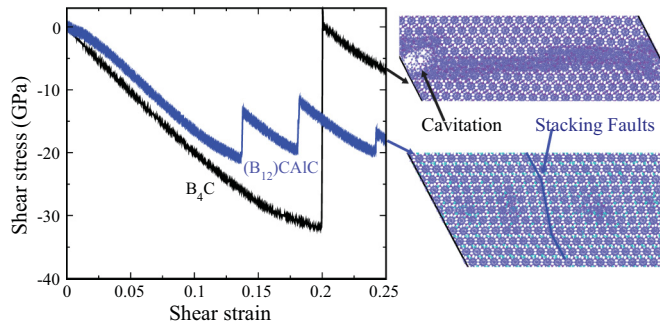


FIG. 2. Shear-stress-shear-strain curves for B_4C and $(B_{12})CAIC$ at finite shear deformation and the atomistic structures at 0.25 shear strain. The solid blue line represents the stacking fault (SF) layers. Only the local structures related to amorphization and SF formation are displayed here, and the detailed structure evolutions for B_4C and $(B_{12})CAIC$ are illustrated in Figs. 3 and 4, respectively.

directly from nanoindentation and high-resolution transmission electron microscopy experiments [8].

The experimentally observed amorphous shear bands in B_4C are $\sim 2\text{--}3$ nm in width and several hundred nanometers in length. Simulating the formation of amorphous band formation requires a supercell with cell length ~ 10 nm perpendicular to the amorphous band, which is beyond the capacity of QM simulations. The intriguing bonding character in B_4C and other icosahedral solids makes it challenging to develop a classical FF for them. To describe the atomistic interaction in both B_4C and Al-doped B_4C systems, the ML-FF is developed based on the atomic force, system energy, and virial stress obtained from extensive QM-MD simulations. The ML-FF represents the potential energy surface of atomistic systems as a sum of “atomic energy” that depend on the coordinates of the atoms in a symmetry-preserving way [46,47].

To illustrate the shear-induced amorphization process in B_4C , a supercell was constructed with the dimensions of $12.5 \times 12.2 \times 3.1$ nm along [100], [001], and [010] lattice directions. The system was first equilibrated at room temperature for 100 ps. Then [100] is aligned along the x direction, and [001] is in the xy plane. Finally, finite shear deformation is applied in the xy plane to mimic the shear deformation along the slip system (001)[100]. The strain rate is $5.0 \times 10^8 \text{ s}^{-1}$; that is comparable to the shock compression [9]. The initial structure for shear deformation is illustrated in Fig. S2(a) of the SM [41]. During the shear deformation, the stresses along the other five directions are relaxed using the NPT ensemble to mimic the ideal shear deformation. The stress components of the other five directions fluctuate around zero during the shear deformation, as shown in Fig. S3 of the SM [41].

Figure 2 displays the shear-stress-shear-strain relationship of B_4C along the most plausible slip system (001)[100] (black curve). The crystalline B_4C deforms elastically to ~ 0.15 shear strain. Then the slope of the stress-strain curve slightly decreases, yet the structure does not exhibit significant change. As the shear strain increases to ~ 0.2 , the shear stress drops abruptly from the critical stress of ~ 32 to ~ 0 GPa, indicating a brittle failure in B_4C . The failed structure at 0.25 shear strain, displayed in Fig. 2, shows an amorphous shear band along the (001) shear plane, which resembles the

experimental transmission electron microscopy observation [8]. This confirms that the amorphous shear band is the major failure mechanism of B_4C [7–16]. It is worth noting that the formed amorphous shear band in this paper is not uniformly distributed along the shear plane, as seen in Fig. 2. Some regions have only two amorphous icosahedral layers, while others cross four layers. A cavity is present in the four-layer amorphous region, suggesting a close relationship between amorphization and brittle failure. The ideal shear stress for B_4C is 32 GPa from the simulations, which is close to the critical shear stress of popping up dislocations in single-crystal B_4C measured from experiments [48]. This indicates that the direct amorphization in B_4C along the slip system (001)[100] is a competitive deformation mechanism to the dislocation mediated amorphization along other slip systems [48].

To illustrate the amorphization and failure mechanism of B_4C , detailed analyses on the MD trajectory were performed from 0.199 to 0.2015 shear strain. Figure. 3(a) displays the stress-strain relationship in this strain interval. The strain at 0.199 strain does not show obvious bond breaking, as shown in Fig. 3(b). As the shear strain increases to 0.19945, the icosahedral-icosahedral B-C bonds break among a few icosahedra into two adjacent layers [Fig. 3(c)], yet this does not cause a significant drop of shear stress. The initial icosahedral-icosahedral B-C bond breaking is consistent with our previous DFT simulations [12], demonstrating the accuracy of this ML-FF. Then the icosahedra start to collapse, and the amorphization propagates along opposite directions in the two adjacent layers at 0.1996 shear strain [Fig. 3(d)]. Next, the propagation of amorphization in the upper layer stops after deconstructing a couple of icosahedra and transforms to the above icosahedral layer. Similarly, the amorphization in the lower layer extends to the below icosahedral layer without further deconstructing icosahedra in the initial layer. This leads to the presence of disintegrated icosahedra in four layers, as shown in Fig. 3(e). This propagation of amorphization only leads to a small drop of shear stress to ~ 25 GPa. Due to the PBC in the MD supercell, the upper amorphous layers meet the lower amorphous layers at 0.200 strain, causing the deconstruction of icosahedral in all four layers [Fig. 3(f)]. This makes the shear stress drop to ~ 15 GPa. Finally, a cavity forms in the four-layer amorphous region at 0.2005 strain [Fig. 3(g)], relaxing the shear stress quickly to ~ 0 GPa. The structure remains unchanged up to 0.2015 shear strain, as shown in Fig. 3(h). A movie showing the detailed amorphization and failure process can be found in the SM [41].

To investigate the temperature, pressure, and shear-stress evolution during the amorphization, a binning analysis was performed, and the results are displayed in Figs. S4–S6 of the SM [41]. Figure S4(a) of the SM [41] shows that the temperature does not significantly increase as the initial deconstruction of icosahedra. As the amorphization propagates across the whole simulation cell, the temperature significantly increases to ~ 2200 K, as shown in Fig. S4(b) of the SM [41]. Then the temperature drops along the amorphous region since the temperature is controlled by a thermostat (Fig. S4(c) of the SM [41]). It is worth noting that the melting temperature of B_4C is ~ 2700 K [1], which is higher than the increased temperature in this paper. This suggests that the failure process in this paper is the mechanical stress-induced amorphization.

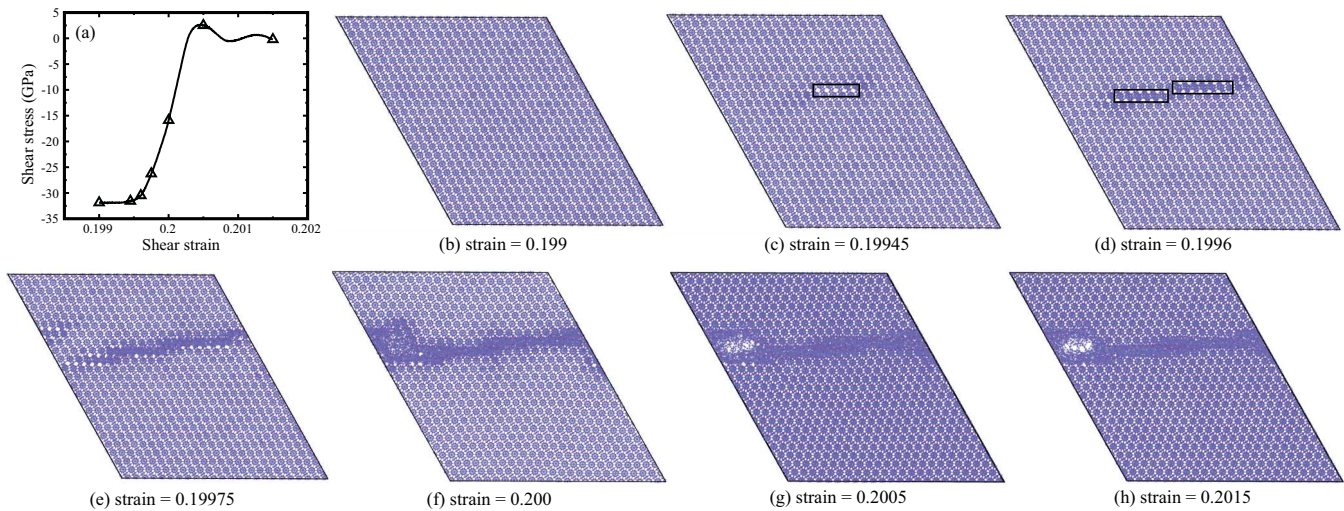


FIG. 3. The amorphization and failure mechanism of B_4C from 0.199 to 0.2015 shear strain. (a) The shear-stress-shear-strain relationship and the following examined structures labeled with triangle symbols. (b) The structure at 0.199 strain without obvious bond breaking. (c) The initial bond breaking at 0.19945 strain displayed in the rectangular region. (d) The structure at 0.1996 strain showing the propagation of amorphization along opposite directions in the rectangular region. (e) The structure at 0.19975 strain displaying the amorphization transforms to other icosahedral layers. (f) The structure at 0.2 strain showing the formation of an amorphous region across four icosahedral layers. (g) Cavitation formation in the amorphous region at 0.2005 strain. (h) The amorphous band at 0.2015 strain like (g).

However, the increased temperature during the amorphization softens the bonding in B_4C and may promote cavitation and failure in the amorphous region. The shear-stress profile, displayed in Fig. S5 of the SM [41], indicates that the amorphization causes the relaxation of shear stress. In addition, the pressure increases in the amorphous region (Fig. S6 of the SM [41]), which is consistent with the fact that the amorphous region has a higher density than the crystalline region.

C. Shear deformation of Al-doped B_4C

A recent experimental study suggested that 1–5 at. % Al can be incorporated into boron carbide through arc-melting, leading to a similar crystal structure as B_4C and lattice expansion [49]. However, the structure of the Al-doped BC system is not well characterized, in contrast to extensive studies on B_4C . Several possible structures are examined in this paper based on previous studies [50,51]: $(B_{12})CAIC$, $(B_{12})CAIB$, and $(B_{11})CAIC$. DFT simulations indicated that $(B_{12})CAIC$ is the most plausible structure with the heat of formation of 1.28 eV taking face-centered cubic Al, α - B_{12} , and graphite crystal as the reference structures. For comparison, the $(B_{12})CAIB$ and $(B_{11})CAIC$ structures have a smaller heat of formation of 0.82 and 0.24 eV, respectively. Therefore, the $(B_{12})CAIC$ structure [Fig. 1(b)] is selected for the finite shear deformation along the same slip system as B_4C . It is worth noting the B/C ratio in $(B_{12})CAIC$ is 6.0, which is >4.0 in B_4C , which is consistent with the experimental observation that Al can only be incorporated into B_4C with the addition of B [49]. The $(B_{12})CAIC$ is relaxed at room temperature and then is sheared along the same slip system (001)[100], as displayed in Fig. S2(b) of the SM [41].

The deformation mechanism for $(B_{12})CAIC$ is drastically in contrast with B_4C . In contrast to B_4C , the shear-stress-shear-strain relationship of $(B_{12})CAIC$ (blue curve in Fig. 2)

exhibits a different behavior—the shear stress only drops from critical stress of ~ 20 to ~ 13 GPa, while it continuously increases to ~ 20 GPa with the same stress-strain slope as the perfect crystal. This suggests that $(B_{12})CAIC$ does not lose the shear strength at finite shear deformation. Up to 0.25 strain, the shear stress drops and increases three times, but no amorphous shear band is present in $(B_{12})CAIC$ at 0.25 shear strain (Fig. 2). Instead, a SF layer is present across six icosahedral layers, suggesting that the relaxation of the shear stress is accomplished through SF formation in $(B_{12})CAIC$, quite distinct from the amorphization in B_4C .

Figure 4 illustrates the detailed deformation process of forming SFs in the shear strain ranging from 0.1385 to 0.141. The shear-stress-shear-strain relationship, displayed in Fig. 4(a), shows the shear-stress relaxation from ~ 21 to ~ 14 GPa in this process. The structure at 0.139 shear strain is elastically deformed from the perfect crystal without bond breaking, as shown in Fig. 4(b). When the shear strain increases to 0.1395, one icosahedral layer slips relative to its adjacent layers [Fig. 4(c)], releasing the shear stress from ~ 21 to ~ 17.5 GPa. Since the C-Al-C chain is weaker than the bonding in (B_{12}) icosahedron, the icosahedral slip is observed in the $(B_{12})CAIC$ system rather than the disintegration of icosahedra. Two adjacent icosahedra along the slip layer are deconstructed, while the cage collapse is confined to this very local region. Then an additional icosahedral layer above the SF layer starts to slip, forming a three-layer SF structure, Figs. 4(d) and 4(e), relaxing the shear stress to ~ 14 GPa. Finally, the SF structure remains stable with the increased shear strain [Fig. 4(f)]. More SF layers form with the further increased strain, leading to a total of six SF layers at 0.25 shear strain (Fig. 2). The detailed process of SF formation can be found in the movie of the SM [41].

The SF formation due to the icosahedral slip under high strain rate deformation has significant implications on

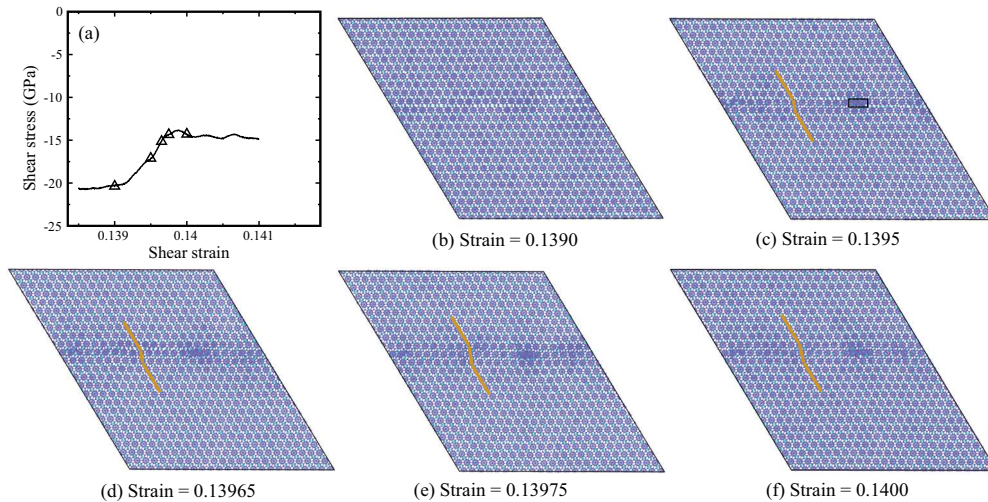


FIG. 4. The formation of stacking faults (SFs) in $(B_{12})CAIC$ from 0.1385 to 0.141 shear strain. (a) The shear-stress-shear-strain relationship and the examined structures are labeled with the triangle. (b) The structure at 0.139 strain without obvious bond breaking. (c) The initiation of the icosahedral slip at 0.1395 strain with two adjacent icosahedra deconstructed in the rectangular region. (d) The structure at 0.13965 strain showing one additional icosahedral layer slips. (e) The structure at 0.13975 strain displaying the formation of three-layer SF structure. (f) The SF structure remains stable at 0.1400 strain. The solid yellow lines represent the SF structures.

materials design to improve the ductility of superhard B_4C [18]. The icosahedral slip is facilitated in the $(B_{12})CAIC$ system because of the relative weak C-Al chain compared with the cage bonding. The modification of chain structure changes the deformation mechanism from amorphization in B_4C to SF formation in $(B_{12})CAIC$. It is expected that the ductility of B_4C will be significantly improved through Al doping that is achievable experimentally [49]. This paper suggests that future materials design can focus on increasing the icosahedral slip to improve the ductility of boron carbide and related icosahedral solids.

This paper focuses on the amorphization process of B_4C under ideal shear deformation as well as the suppression of local amorphization by Al dopant. The deformation mechanism under a more complex situation will be explored in the future, practically under shock compression.

IV. CONCLUSIONS

In summary, this paper illustrates the amorphization and failure process of B_4C under finite shear deformation from

the ML-FF MD simulations. The amorphous band initiates from the deconstruction of icosahedra in two adjacent layers, and then it propagates to other neighbor layers, leading to the formation of a four-layer amorphous band. Finally, a cavity is present in the amorphous band, releasing the shear strength and leading to brittle failure. In contrast, the $(B_{12})CAIC$ system exhibits a different deformation mechanism in which the icosahedral slip causes the formation of SF, releasing the shear strength without deconstructing the icosahedral clusters. This identified deformation mechanism in $(B_{12})CAIC$ suggests that adding Al into B_4C can significantly improve the ductility.

ACKNOWLEDGMENTS

This paper is supported by National Science Foundation with Funding No. CMMI-1727428. The authors would also like to acknowledge the support of Research & Innovation and the Cyberinfrastructure Team in the Office of Information Technology at the University of Nevada, Reno, for facilitation and access to the Pronghorn High-Performance Computing Cluster.

[1] V. Domnich, S. Reynaud, R. A. Haber, and M. Chhowalla, Boron carbide: structure, properties, and stability under stress, *J. Am. Ceram. Soc.* **94**, 3605 (2011).
 [2] F. Thevenot, Boron carbide—a comprehensive review, *J. Eur. Ceram. Soc.* **6**, 205 (1990).
 [3] J. L. Hoard and R. E. Hughes, in *The Chemistry of Boron and Its Compounds*, edited by E. L. Muetterties (Wiley, New York, 1967).
 [4] A. K. Suri, C. Subramanian, J. K. Sonber, and T. S. R. Ch. Murthy, Synthesis and consolidation of boron carbide: a review, *Int. Mater. Rev.* **55**, 4 (2010).
 [5] J. Deng, Erosion wear of boron carbide ceramic nozzles by abrasive air-jets, *Mater. Sci. Eng. A* **408**, 227 (2005).
 [6] D. E. Grady, Hugoniot equation of state and dynamic strength of boron carbide, *J. Appl. Phys.* **117**, 165904 (2015).
 [7] M. W. Chen, J. W. McCauley, and K. J. Hemker, Shock-induced localized amorphization in boron carbide, *Science* **299**, 1563 (2003).
 [8] K. M. Reddy, P. Liu, A. Hirata, T. Fujita, and M. W. Chen, Atomic structure of amorphous shear bands in boron carbide, *Nat. Commun.* **4**, 2483 (2013).
 [9] S. T. Zhao, B. Kada, B. A. Remington, J. C. LaSalviac, C. E. Wehrenberg, K. D. Behler, and M. A. Meyers, Directional amorphization of boron carbide subjected to laser shock compression, *Proc. Natl. Acad. Sci. USA* **113**, 12088 (2016).

- [10] M. W. Chen and J. W. McCauley, Mechanical scratching induced phase transitions and reactions of boron carbide, *J. Appl. Phys.* **100**, 123517 (2006).
- [11] D. Gosset, S. Miro, S. Doriot, G. Victor, and V. Motte, Evidence of amorphisation of B₄C boron carbide under slow, heavy ion irradiation, *Nucl. Instrum. Methods Phys. Res., Sect. B* **365**, 300 (2015).
- [12] Q. An and W. A. Goddard III, Atomistic Explanation of Shear-Induced Amorphous Band Formation in Boron Carbide, *Phys. Rev. Lett.* **113**, 095501 (2014).
- [13] Q. An and W. A. Goddard III, Atomistic Origin of Brittle Failure of Boron Carbide from Large-Scale Reactive Dynamics Simulations: Suggestions toward Improved Ductility, *Phys. Rev. Lett.* **115**, 105501 (2015).
- [14] G. Fanchini, J. W. McCauley, and M. Chhowalla, Behavior of Disordered Boron Carbide under Stress, *Phys. Rev. Lett.* **97**, 035502 (2006).
- [15] D. E. Taylor, J. W. McCauley, and T. W. Wright, The effects of stoichiometry on the mechanical properties of icosahedral boron carbide under loading, *J. Phys.: Condens. Matter* **24**, 505402 (2012).
- [16] J. Li, S. Xu, J. Zhang, and L. Liu, First-principles predicting improved ductility of boron carbide through element doping, *J. Phys. Chem. C* **125**, 11591 (2021).
- [17] Q. An, K. M. Reddy, J. Qian, K. J. Hemker, M. W. Chen, and W. A. Goddard III, Nucleation of amorphous shear bands at nanotwins in boron suboxide, *Nat. Commun.* **7**, 11001 (2016).
- [18] Y. Shen, J. Fuller, and Q. An, Mitigating the formation of amorphous shear band in boron carbide, *J. Appl. Phys.* **129**, 140902 (2021).
- [19] S. Xiang, L. Ma, B. Yang, Y. Dieudonne, G. M. Pharr, J. Lu, D. Yadav, C. Hwang, J. C. LaSalvia, R. A. Haber, K. J. Hemker, and K. Y. Xie, Tuning the deformation mechanisms of boron carbide via silicon doping, *Sci. Adv.* **5**, eaay0352 (2019).
- [20] A. Chauhan, M. C. Schaefer, R. A. Haber, and K. J. Hemker, Experimental observations of amorphization in stoichiometric and boron-rich boron carbide, *Acta Mater.* **181**, 207 (2019).
- [21] K. Y. Xie, K. Kuwelkar, R. A. Haber, J. C. LaSalvia, K. J. Hemker, and R. Hay, Microstructural characterization of a commercial hot-pressed boron carbide armor plate, *J. Am. Ceram. Soc.* **99**, 2834 (2016).
- [22] D. Guo, S. Song, R. Luo, W. A. Goddard, M. Chen, K. M. Reddy, and Q. An, Grain Boundary Sliding and Amorphization are Responsible for the Reverse Hall-Petch Relation in Superhard Nanocrystalline Boron Carbide, *Phys. Rev. Lett.* **121**, 145504 (2018).
- [23] Y. Gu, J. X. Liu, F. Xu, and G. J. Zhang, Pressureless sintering of titanium carbide doped with boron or boron carbide, *J. Eur. Ceram. Soc.* **37**, 539 (2017).
- [24] L. Yang, G. Min, H. Yu, J. Han, and Y. B. Paderno, Densification and mechanical properties of CaB₆ with nickel as a sintering aid, *Ceram. Int.* **31**, 271 (2005).
- [25] L. S. Sigl, Processing and mechanical properties of boron carbide sintered with TiC, *J. Eur. Ceram. Soc.* **18**, 1521 (1998).
- [26] Q. An and W. A. Goddard III, Ductility in crystalline boron subphosphide (B₁₂P₂) for large strain indentation, *J. Phys. Chem. C* **121**, 16644 (2017).
- [27] Q. An and W. A. Goddard III, Microalloying boron carbide with silicon to achieve dramatically improved ductility, *J. Phys. Chem. Lett.* **5**, 4169 (2014).
- [28] G. Kresse and J. Hafner, *Ab initio* molecular dynamics for liquid metals, *Phys. Rev. B* **47**, 558 (1993).
- [29] G. Kresse and J. Furthmüller, Efficiency of *ab initio* total energy calculations for metals and semiconductors using a plane-wave basis set, *Comput. Mater. Sci.* **6**, 15 (1996).
- [30] G. Kresse and J. Furthmüller, Efficient iterative schemes for *ab initio* total-energy calculations using a plane-wave basis set, *Phys. Rev. B* **54**, 11169 (1996).
- [31] G. Kresse and D. Joubert, From ultrasoft pseudopotentials to the projector augmented-wave method, *Phys. Rev. B* **59**, 1758 (1999).
- [32] W. G. Hoover, A. J. C. Ladd, and B. Moran, High-Strain-Rate Plastic Flow Studied via Nonequilibrium Molecular Dynamics, *Phys. Rev. Lett.* **48**, 1818 (1982).
- [33] M. Parrinello and A. Rahman, Crystal Structure and Pair Potentials: A Molecular-Dynamics Study, *Phys. Rev. Lett.* **45**, 1196 (1980).
- [34] J. P. Perdew, K. Burke, and M. Ernzerhof, Generalized Gradient Approximation Made Simple, *Phys. Rev. Lett.* **77**, 3865 (1996).
- [35] J. P. Perdew, K. Burke, and M. Ernzerhof, Erratum: Generalized Gradient Approximation Made Simple, *Phys. Rev. Lett.* **78**, 1396(E) (1997).
- [36] A. R. Oganov and V. L. Solozhenko, Boron: a hunt for superhard polymorphs, *J. Superhard Mater.* **31**, 285 (2009).
- [37] R. E. Hughes, C. H. L. Kennard, D. B. Sullenger, H. A. Weakliem, D. Sands, and J. L. Hoard, The structure of β -rhombohedral boron, *J. Am. Chem. Soc.* **85**, 361 (1963).
- [38] Q. An, K. M. Reddy, K. Y. Xie, K. J. Hemker, and W. A. Goddard III, New Ground-State Crystal Structure of Elemental Boron, *Phys. Rev. Lett.* **117**, 085501 (2016).
- [39] A. R. Oganov, J. Chen, C. Gatti, Y. Ma, Y. Ma, C. W. Glass, Z. Liu, T. Yu, O. O. Kurakevych, and V. L. Solozhenko, Ionic high-pressure form of elemental boron, *Nature (London)* **457**, 863 (2009).
- [40] Q. An, Prediction of superstrong τ -boron carbide phase from quantum mechanics, *Phys. Rev. B* **95**, 100101(R) (2017).
- [41] See Supplemental Material at <http://link.aps.org/supplemental/10.1103/PhysRevMaterials.5.103602> for Figs. S1–S6 and two movies displaying the amorphization in B₄C (0.199–0.201 shear strain) and stacking faults formation in (B₁₂)CAIC (0.139–0.140 shear strain), respectively.
- [42] S. Plimpton, Fast parallel algorithms for short-range molecular dynamics, *J. Comp. Phys.* **117**, 1 (1995).
- [43] R. Hill, The elastic behaviour of a crystalline aggregate, *Proc. Phys. Soc., London, Sect. A* **65**, 349 (1952).
- [44] Y. Le Page and P. Saxe, Symmetry-general least-squares extraction of elastic data for strained materials from *ab initio* calculations of stress, *Phys. Rev. B* **65**, 104104 (2002).
- [45] D. C. Rapaport, *The Art of Molecular Dynamics Simulation* (Cambridge University Press, Cambridge, 1995).
- [46] L. Zhang, J. Han, H. Wang, R. Car, and E. Weinan, Deep Potential Molecular Dynamics: A Scalable Model with the Accuracy of Quantum Mechanics, *Phys. Rev. Lett.* **120**, 143001 (2018).
- [47] J. Han, L. Zhang, R. Car, and E. Weinan, Deep potential: a general representation of a many-body potential energy surface, *Commun. Comput. Phys.* **23**, 629 (2018).

- [48] K. M. Reddy, D. Guo, S. Song, C. Cheng, J. Han, X. Wang, Q. An, and M.-W. Chen, Dislocation-mediated shear amorphization in boron carbide, *Sci. Adv.* **7**, eabc6714 (2021).
- [49] S. Xiang, Q. Yang, H. M. Lien, K. Shial, E. Grounske, R. Haber, and K. Y. Xie, The effect of boron and aluminum additions on the microstructure of arc-melted boron carbide, *J. Am. Ceram. Soc.* **103**, 3453 (2020).
- [50] H. Neidhard, R. Mattes, and H. Becher, The production and structure of a boron carbide containing aluminum, *Acta Crystallogr. B* **26**, 315 (1970).
- [51] R. Schmechel, H. Werheit, K. Robberding, T. Lundström, and H. Bolmgren, Ir active phonon spectra of B-C-Al compounds with boron carbide structure, *J. Solid State Chem.* **133**, 254 (1997).